RESEARCH ARTICLE

ADVANCED MATERIALS INTERFACES
Open Access
www.advmatinterfaces.de

Check for updates

AlScN/GaN Multichannel Heterostructures Grown by Metal–Organic Chemical Vapor Deposition

Teresa Duarte, Isabel Streicher, Patrik Straňák, Lutz Kirste, Mario Prescher, Niklas Wolff, Susanne Beuer, Lorenz Kienle, Rüdiger Quay, and Stefano Leone**

GaN-based high-electron-mobility transistors (HEMTs) are essential for high-volume data transmission and energy conversion because of their high breakdown voltages and power density. By vertically stacking multiple 2D electron gases (2DEGs), it is possible to take advantage of the high electron mobility of these heterostructures while increasing the sheet carrier density. Using AlScN as the barrier material can further augment device performance by increasing the sheet charge carrier densities and reducing channel resistance. Given the possibility of lattice-matching of AlScN with GaN, strain-free layers can be grown. Here, the successful growth of multichannel heterostructures with different period combinations by metal–organic chemical vapor deposition (MOCVD) is reported for the first time. A five-period multilayer structure exhibits carrier densities of 2.5×10^{13} cm^{-2}, mobility above 1900 cm^2 V^{-1} s^{-1}, and sheet resistance as low as 129 Ω sq^{-1}.

1. Introduction

The need for reliable, efficient, and sustainable electrical components is continuously rising in our current society. Compared to conventional Si-based devices, nitride semiconductor devices offer efficient power conversion, transmission of larger data volumes, and switching of higher currents.[1–3] In particular, GaN-based high-electron-mobility transistors (HEMTs) are already available on the market as they provide high breakdown voltages, high power density, and output power at higher frequencies.

Despite significant progress in GaN HEMT technology, the fundamental trade-off between charge carrier mobility (μ) and sheet carrier density (n_s) presents a troublesome obstacle to exploiting the full potential of the theoretically available material properties. Innovative design approaches, such as multichannel heterostructures, in which multiple parallel layers confine a 2D electron gas (2DEG), can bypass these limitations by reducing the resistivity of devices while increasing the carrier density. Extensive work has already been reported for multichannel heterostructures based on AlGaN/GaN[4–8] and AlN/GaN,[9,10] enabling higher breakdown voltages and challenging the performance of other wide band gap materials like SiC.[11–14] However, the lattice mismatch between these barrier materials AlGaN and AlN with GaN introduces stress-related defects, restricting the number of channels that can be grown before cracking, and affects the reliability of devices. Therefore, the use of lattice-matched barrier materials such as AlScN emerges as a straightforward strategy for further improvement of multichannel heterostructures.

AlInN has already been explored as a possible barrier material for multichannels because of this characteristic.[15,16] However, one of the main challenges in AlInN growth is the required low deposition temperature, which elevates the impurity concentrations and degrades crystalline quality.[15,17,18] AlScN not only provides lattice matching, as it can be grown at relatively high temperatures (1150 °C). Thanks to its intrinsically high polarization, a higher n_s and a lower channel resistance could be achieved due to the larger gradient of spontaneous polarization at the interface of AlScN and GaN. The addition of AlN interlayers are also implemented in AlScN/GaN heterostructures to improve the transport properties and make the interfaces more abrupt.[19] Moreover, since AlScN has a wider bandgap than AlInN, the electron density in the 2DEG is further increased, and the electron confinement is improved.

Different growth methods have already been employed to investigate the potential of AlScN for various applications. Sputtering is a well-known growth method for AlScN as it can achieve

T. Duarte, I. Streicher[+], P. Straňák, L. Kirste, M. Prescher, R. Quay, S. Leone
Fraunhofer Institute for Applied Solid State Physics (IAF)
Tullastraße 72, D-79108 Freiburg, Germany
E-mail: teresa.duarte@iaf.fraunhofer.de; stefano.leone@iaf.fraunhofer.de

N. Wolff, L. Kienle
Department of Material Science
Kiel University
Kaiserstr. 2, D-24143 Kiel, Germany

S. Beuer
Fraunhofer Institute for Integrated Systems and Device Technology
D-91058 Erlangen, Germany

The ORCID identification number(s) for the author(s) of this article can be found under https://doi.org/10.1002/admi.202500726

[+]Present address: Consiglio Nazionale delle Richerche - Istituto per la Microelettronica e Microsistemi (CNR-IMM), Strada VIII n.5 - Zona Industriale, Catania 95121, Italy

DOI: 10.1002/admi.202500726

ferroelectric and piezoelectric layers.[20–24] However, due to its ballistic nature, the growth of thin and atomically as well as chemically sharp heterostructure interfaces needed for HEMT structures, especially multichannels, has not yet been demonstrated. Furthermore, sputter epitaxy of GaN channel layers is still a technological challenge under development.[25,26] On the contrary, molecular beam epitaxy (MBE) allows precise control of thickness, interface sharpness, and single-crystalline growth. The properties of MBE-grown AlScN films have been extensively reported in the literature,[27–32] and many applications have already been developed, such as ferroelectric-based applications,[33–35] RF filters,[33,36,37] HEMTs,[38–41] to mention the most common. Recently, different groups[42–44] have studied the growth of molecular beam epitaxy (MBE) AlScN multilayers for optoelectronic applications. Nguyen et al. investigated the lattice matching conditions of MBE-grown AlScN on GaN, which was found to be around 11%.[44] The excellent electrical properties displayed by their AlScN/GaN multichannel heterostructures hint at the potential of a novel strategy for high-power devices with high breakdown voltages and low on-resistance. A possibility to bring this type of structure to further relevance and make it industrially exploitable is to grow them by metal-organic chemical vapor deposition (MOCVD), as it allows for faster growth of the whole stack using industry-standard equipment, and it provides superior uniformity on large substrates. Additionally, MOCVD uses multiwafer reactors, which provide higher productivity compared to MBE.

The growth of AlScN layers by MOCVD is an arduous task due to the low vapor pressure of commercial precursors. To overcome the several difficulties MOCVD-grown AlScN films face, Leone et al.[45,46] proposed modifications to a commercial reactor, successfully demonstrating the growth of single-crystalline layers and the first AlScN/GaN heterostructures for HEMTs. Furthermore, ferroelectric switching,[47] BAW resonators,[48,49] and AlScN/GaN HEMTs[50] grown by MOCVD have also been reported in the literature. It has been proven to be quite challenging to grow high-quality GaN layers on AlScN, yet recently, Streicher et al.[51] demonstrated the growth of GaN cap layers on AlScN. The accomplishments shown in this work enabled the growth of AlScN/GaN multichannels by MOCVD.

In this work, we demonstrate for the first time the growth of AlScN/GaN multichannel heterostructures by MOCVD. We investigated the impact of channel thickness and the number of periods composed of AlScN barrier and GaN channel on the transport properties. For this purpose, structures with variable periods, channel thickness, and Sc-content were grown on (0001) Al_2O_3 and semi-insulating (SI) 4H-SiC substrates. Growth experiments were conducted targeting a smooth morphology, sharp interfaces, and high structural quality. Eventually, promising heterostructures suitable for transistor fabrication were achieved and are discussed in this work.

2. Results and Discussion

Though infinite layers could theoretically be grown, this is not trivial in practice: the Sc concentration for lattice matching with GaN is a topic of ongoing debate, and achieving optimal growth conditions requires significant effort. To achieve these, we systematically studied key parameters including the thickness of the channel layers, the number of periods, interface management, and the impact of the substrate with different off-cuts. 1D numerical Schrödinger–Poisson simulations were performed to corroborate the studies.

Table 1. Properties of the three-period AlScN/GaN multichannel heterostructures with different channel thickness on Al_2O_3 substrates. Electrical properties obtained by contactless Hall effect measurements. The RMS values presented are for the 10×10 μm^2 scans obtained by AFM.

Channel thickness [nm]	R_{sh} [Ω sq^{-1}]	n_s (10^{13} cm^{-2})	μ [cm^2 V^{-1} s^{-1}]	RMS [nm]
15	544	1.17	992	1.09
25	334	1.57	1194	2.14
40	253	1.96	1267	3.53
65	278	3.76	618	2.41

2.1. Channel Thickness Variation

An important aspect when growing this type of structure is the channel thickness, as it strongly impacts the electrical performance. A way to increase mobility is to use thicker channels, as thicker layers have better crystalline quality and, consequently, exhibit fewer scattering effects. On the other hand, thinner GaN channels are advantageous as a larger number of 2DEGs can be stacked on top of each other at a thinner total thickness. Note that the total stack thickness should be considered since contacting and controlling all 2DEGs is challenging and requires adapted device architectures. Hence, a compromise must be found between the total thickness and the achieved electrical characteristics.

One of the requirements for HEMTs is to have a semi-insulating buffer to suppress leakage current. This is typically achieved by doping GaN layers with deep acceptors such as Fe or C. Since our structures use an Fe-doped GaN buffer, a thick undoped layer must be grown on top of it to suppress the memory effects that arise from the Fe diffusion.[52] For the subsequent channel layers, the channel thickness can be chosen without constraints. We experimented with four different GaN channel thicknesses from 15 to 65 nm, while keeping the AlScN barrier layers constant at 10 nm and the Sc content between 9% and 12% in the barriers. **Table 1** presents the room temperature (RT) electrical characteristics and assessment of the surface morphology of three-period multichannel heterostructures with different channel thicknesses. With thinner channels, the 2DEG wave functions are firmly close to the barrier interfaces, which increases interface roughness scattering, and in turn reduces electron mobility.[15] Additionally, the total structure thickness remains low. With increasing channel thickness, n_s likewise increases: 1.17×10^{13} cm^{-2} for 15 nm channel, and up to 3.76×10^{13} cm^{-2} for 65 nm channel. A mobility increase with thickness was also observed (e.g.: 992 cm^2 V^{-1} s^{-1}) with a 15 nm channel, up to 1267 cm^2 V^{-1} s^{-1} with a 40 nm channel), yet it decreased for the thickest channel (65 nm). At this stage, it was not clear what the mechanisms were behind the drop in mobility for the 65 nm channel. Strain relaxation and/or dislocation formation can be possible causes; nevertheless, further investigation is needed (growth optimization, TEM analysis).

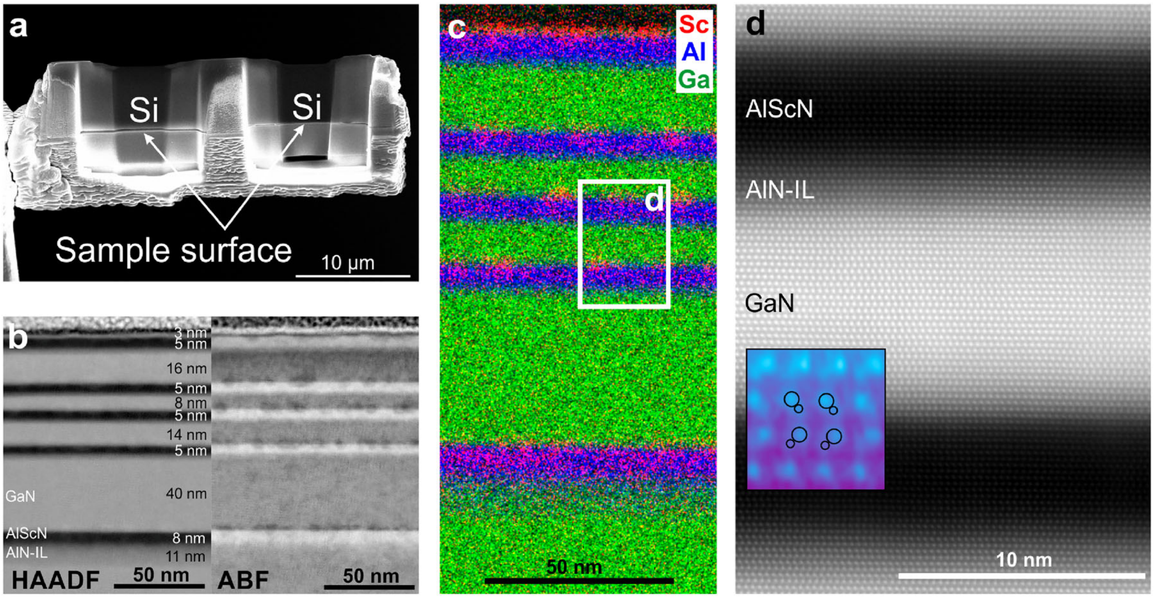

Figure 1. a) Prepared TEM Lamella of a five-period $AlSc_{9\text{-}11\%}N/GaN$ multichannel heterostructure on Al_2O_3. b) HAADF/ABF-STEM images of the periodic multilayer. c) STEM-EDS elemental mapping showing the elemental distribution across the heterostructure. Al: blue, Sc: red, Ga: green. d) HRSTEM image of the internal interfaces in [2-1-10] orientation. (Inset: False-colored image with inverted contrast showing the metal-polar unit-cell orientation within the AlScN layer).

2.2. AlScN/GaN Interfaces

The quality of all crystalline interfaces is denoted as crucial in defining the electrical characteristics. To assess the impact of the changes in the carrier gas on the structural characteristics of the heterostructures, TEM analysis was used for a five-period multichannel heterostructure on Al_2O_3 with Sc composition between 9% and 11%. **Figure 1a** shows the thin cross-section specimen prepared by using a thin Si-Cube from the "flying cube strategy" as a protection layer for rippling-free preparation of harder material.[53] The overview HAADF/ABF-STEM images (Figure 1b) demonstrate the 2D growth of the periodic multichannel structure with 5 nm thin AlScN layers and GaN layers of varying thickness. The variations observed in both the barriers and channels thicknesses stem from the non-uniformity of this sample. This was likely due to a particle below the wafer, causing a non-uniform temperature profile and, consequently, a non-uniform alloy composition (Figure S1, Supporting Information). The ABF-STEM contrast image and the EDS map (Figure 1c) reveal chemical inhomogeneities identified as Sc-rich grains with cubic structure, which clot at the AlScN/GaN interfaces (cf. Figure S2, Supporting Information). What is noticeable from the EDS map is the significant presence of Sc-clusters in all barriers except the first one, which was grown with H_2 as the carrier gas. While N_2 is needed to prevent etching effects and for the growth of smooth upper GaN channel layers, it hinders the mobility of the Sc atoms in the growth of AlScN, leading to an increased appearance of clusters at the AlScN/GaN interface. Atomic-resolution micrographs (Figure 1d) of the internal interfaces show areas of the epitaxial heterostructure in $[2\bar{1}\bar{1}0]$ crystal orientation in the absence of structural defects and confirm the metal-polar growth orientation. The in-plane and out-of-plane strain distribution across the multichannel was examined by performing geometric phase analysis on non-rigidly aligned STEM image stacks, reducing effects of sample drift and scan distortions.[54] The out-of-plane (ε_{zz}) strain map and profile are shown in Figure S3a,b (Supporting Information). The observed difference in the z-direction of about –4–5% agrees with the change of the c lattice parameter of an AlScN film. Interestingly, we observe an increase in the vertical strain component by ≈+1% across the GaN channel layers. The in-plane strain variance across the AlScN/GaN layers is on the same order as the noise in the GaN layers. Local differences in the strain distributions (marked regions) suggest the position of Sc-rich clusters sitting at the interfaces. Therefore, we conclude that the AlScN layers grow pseudomorphically strained (<1% deviation) with about the same in-plane lattice parameter as the GaN layers. The 3 nm thin crystalline GaN capping layer is demonstrated to be effective in preventing the oxidation of the underlying AlScN-barrier layer, as visible from the oxygen (O-K) EDS map displayed in Figure S4 (Supporting Information). However, defects in the GaN capping layer (Figure S5, Supporting Information) result in local oxidation of the barrier layer underneath.

2.3. Impact of Substrate Type and Off-Cut

The substrate used greatly impacts the quality of the heterostructures. Although Al_2O_3 substrates are more cost-effective, they present a high lattice mismatch with GaN and a lower thermal conductivity when compared to 4H-SiC substrates. Five-period multichannel heterostructures with 10 nm thick $AlSc_{0.08}N$ barriers, 40 nm GaN channels, and GaN cap were grown on Al_2O_3 and S.I. 4H-SiC substrates. When transferring the growth process optimized on the off-cut sapphire substrates to the on-axis 4H-SiC substrate, the morphology turned out rougher,

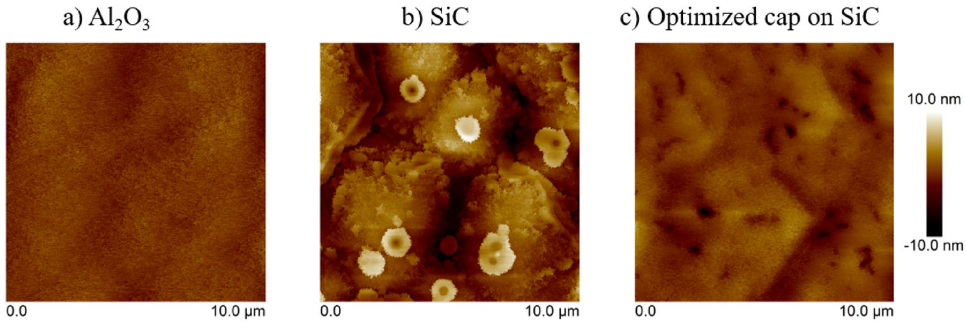

Figure 2. AFM 10 × 10 µm^2 scans of the surface morphology of five-period multichannel heterostructures with 10 nm thick $AlSc_{0.08}N$ barriers, 40 nm GaN channels, and GaN cap on different substrates: a) Al_2O_3, b) 4H-SiC, and c) 4H-SiC with optimized growth conditions for the GaN cap (3.3 nm).

as shown in **Figure** 2a,b, respectively. As expected, the substrate off-cut, which is different for the two substrates, Al_2O_3 has a 0.3° off-cut while 4H-SiC has 0.05°, plays an important role. The off-cut and terrace width require different supersaturation and growth temperatures to increase the adatoms' mobility. At the same time, the inclusion of different crystal structures has to be avoided, making it a frequent challenge in heteroepitaxial growth of semiconductors.[55–59] Furthermore, the substrates present different polishing, thermal conductivities, and strain profiles, all of which also impact the growth. For our multichannel heterostructures, to achieve a smooth surface on 4H-SiC, the cap growth temperature and the thickness of the AlN IL before the cap were increased. Additionally, the supersaturation for the cap was further decreased. With this, an RMS value of 0.9 nm in a 10 × 10 µm^2 scan area (Figure 2c) was achieved. The GaN cap thickness for the optimized growth conditions was 3.3 nm.

2.4. Effect of the Number of Periods

The sheet carrier density increases linearly with the number of channels,[6,44] so aiming to improve the electrical characteristics of the heterostructures, the 40 nm thick channel was selected for the growth of five-period structures on 4H-SiC substrates. These structures presented low R_{sh} (<150 Ω sq^{-1}) while maintaining high mobility (>1300 cm^2 V^{-1} s^{-1}) and smooth morphologies (<1 nm in a 10 ×10 µm^2 scan area) (Figure 2c).

The HRXRD reciprocal space map (RSM) of the $11\bar{2}4$ reflection range (**Figure** 3), measured with a steep incidence and a shallow exidence, shows superlattice peaks of AlScN and GaN layers aligned vertically on the crystal truncation rod in the RSM for the five-period heterostructure, indicating that the multilayers were pseudomorphically grown and confirming good structural quality.

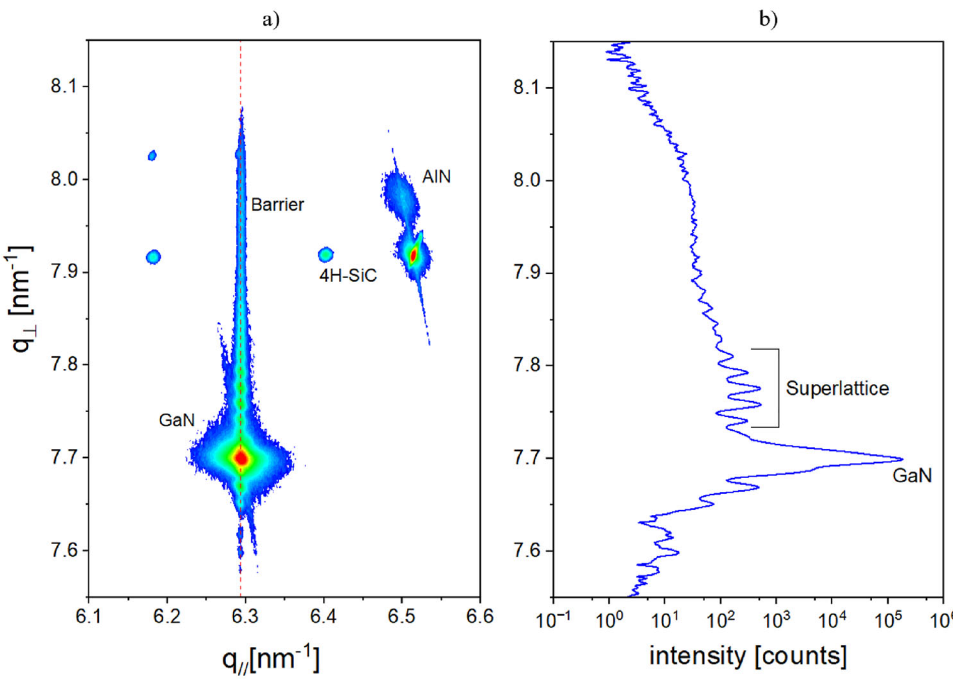

Figure 3. a) RSM scan of the $11\bar{2}4$ reflection range showing that the five-period heterostructure is fully strained, and b) the vertical scan through the RSM of $11\bar{2}4$.

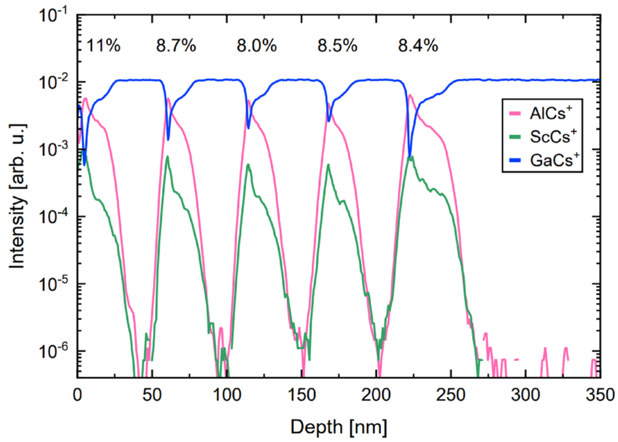

Figure 4. ToF-SIMS depth profile of a five-period AlScN/GaN multichannel heterostructure grown on SiC substrate. Ions were detected in positive ion mode as MCs^+ cluster ions, with M representing the element of interest. The obtained signals were normalized to the Cs^+ signal to correct for matrix effects. The Scandium content of each channel is indicated above it.

Figure 4 shows the ToF-SIMS depth profile of a five-period sample grown on a 4H-SiC substrate with the optimized morphology. The layers are resolved and show consistent Sc composition (≈8%) and thickness for the different barriers. The AlGaScN tail observed in the $AlCs^+$, $GaCs^+$, and $ScCs^+$ signals arises from the diffusion effects caused by the high growth temperature used, causing unintentionally formed interlayers, as seen in the previous MOCVD–AlScN reports.[19,60] Finally, the last barrier layer is followed by a thin cap, which gives less time and lower thermal budget for Sc atoms to diffuse before the cool-down process. Instead, all the other barriers are followed by thicker layers; therefore, they also experience higher thermal budgets. Hence, the observed difference in Sc concentration between the intermediates (≈8%) and the final barrier (11%). This heterostructure presented a R_{sh} of 129 Ω sq^{-1}, n_s of 2.5 × 10^{13} cm^{-2}, and mobility of 1911 cm^2 V^{-1} s^{-1}.

To further study the effects of strain on MOCVD-grown multichannel heterostructures, a ten-period structure was grown on a 4H-SiC substrate. The growth of structures with periods higher than five poses several challenges. Not only should the Sc-content be set to the lattice match condition of AlScN to GaN, but also strain compensation strategies such as tuning the AlN-interlayer thickness, compositional grading, and reducing the difference in growth temperature for the channels and the barriers, may be necessary to achieve beyond five-period heterostructures. The ten-period structure grown presented several cracks, indicating that the Sc concentration of 8% being used was not that of the lattice match to GaN. Achieving a constant Sc composition for the barriers in MOCVD-grown layers requires further tuning of the growth conditions, as the diffusion effects are strongly pronounced. Recently, the lattice match composition range for MBE-grown films was identified to be within 9–11%.[44] However, the growth conditions of MBE and MOCVD-grown films greatly differ, and the significant interdiffusion effects from MOCVD growth modify the strain state. Indeed, with the use of the lattice-matched Sc concentration, more periods could possibly be grown by MOCVD. Considering this, a five-period heterostructure with higher Sc content (≈11%) was grown. The sample presented a R_{sh} of 151 Ω sq^{-1}, n_s of 3.15× 10^{13} cm^{-2}, and mobility of 1313 cm^2 V^{-1} s^{-1}. However, surface morphology was much rougher (RMS = 2.91 nm in a 10 ×10 μm^2 scan area, Figure S6, Supporting Information), requiring further optimization.

3. Discussion

When plotting the μ versus the n_s of the heterostructures, see **Figure 5**, we see that as the channel thickness increases, so does μ and n_s until the channel thickness is 65 nm, where the electrical performance shows a different behavior. By increasing the number of periods, the R_{sh} of the heterostructures are significantly lower. The samples grown on Al_2O_3 experienced an increase of n_s when the number of channels was increased from three to five. However, when we compare a single-channel structure and a multichannel structure grown on 4H-SiC, there is no significant increase in n_s, but instead in mobility. However, these results were obtained with contactless Hall measurements, which may be affected by physical effects that can alter the real value. To further explore this phenomenon, Schrödinger–Poisson 1D simulations of a five-period structure were done. **Figure 6a** presents a schematic diagram of the simulated heterostructure, where the thickness and Sc concentrations were taken from the ToF-SIMS results, and for simplicity, the interlayers and diffusion were neglected. Looking at the simulation of the charge carrier distribution in Figure 6b, the n_s distribution throughout the channels is quite homogeneous despite the slight differences in thickness and barrier composition. While we did not perform experimental studies regarding the channel thickness for a 5-period heterostructure, we observed through simulations that if the channels are too thin, the conduction band edge gets pulled upwards, significantly decreasing the 2DEG density. What is striking is that, according to the simulations, a 2D hole gas (2DHG) should be present. This could be a possible explanation as to why the heterostructures did not present a substantial increase in the carrier density. The reported values of n_s for the MBE-grown AlScN multilayers are 4.63 × 10^{13} cm^{-2} and 8.24 × 10^{13} cm^{-2} with ten- and 20-periods, respectively.[44] In the 2DHG, the simulated hole density is of 1.43 × 10^{14} cm^{-2}, while the electron density in the 2DEG is 1.82 × 10^{14} cm^{-2}, with the net total density being 3.8 × 10^{13} cm^{-2} for the simulated MOCVD-grown heterostructure. Even though 2DHG in AlScN/GaN heterostructures has not been experimentally shown for this kind of heterostructure, their contribution cannot be excluded. Another argument for the low n_s could stem from the added presence of Ga in our barrier, as it is known to decrease it when replacing Sc atoms.[61] It can be hypothesized that with multiple channels, there is a better distribution of the electrons throughout the channels when the density is comparable to that of a single channel, hence the high mobility exhibited by our samples. Indeed, when compared to the 5-period MBE-grown AlScN/GaN multichannel reported in the literature,[62] the mobility of our samples is higher. While the mobility of the MOCVD-grown AlScN/GaN structure was among the highest reported for this type of structure, compared to 5-period heterostructures reported in the literature with AlGaN/GaN,[5,63] AlN/GaN,[10] and AlInN/GaN,[16] the transport properties of the structure still require tuning (Figure 5).

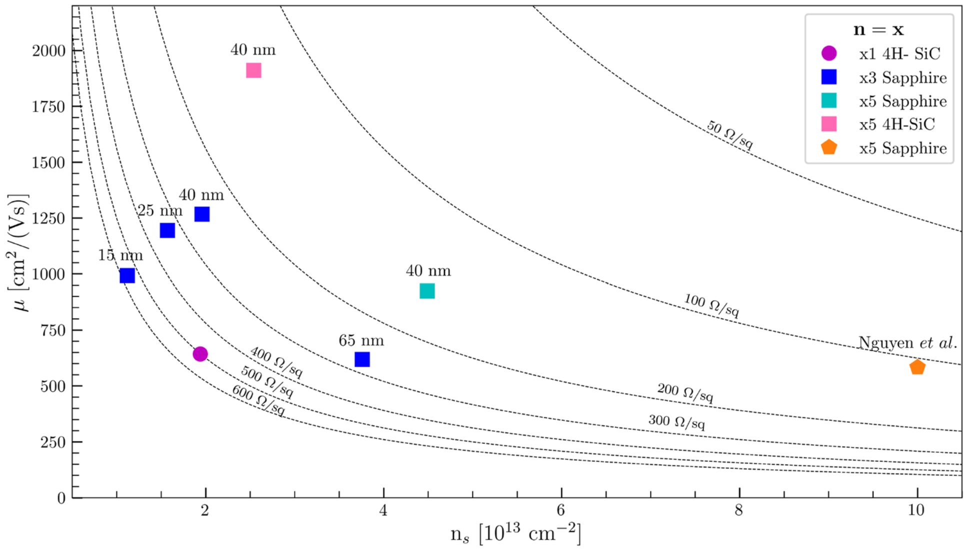

Figure 5. Electrical performance in contactless Hall measurements at RT of an AlScN/GaN single channel heterostructure and multichannel heterostructures with different n-periods on Al_2O_3 and 4H–SiC substrates. The numbers next to the data points indicate the channel thicknesses. Previously published results on AlScN/GaN multichannel heterostructures are shown for comparison.[62] Lines of constant sheet resistance are indicated.

Nevertheless, the presented results already showcase the potential of AlScN/GaN multichannel heterostructures, with further room for improvement still possible.

4. Conclusion

AlScN/GaN multichannel heterostructures were grown for the first time by MOCVD. These structures presented smooth morphologies, high mobility, and low sheet resistance. The thickness of the channels has been shown to have a strong impact on the electrical characteristics of the samples, with resistance increasing and mobility decreasing above 65 nm channel thickness. The growth temperature and the supersaturation during growth heavily impacted surface morphology. By increasing the surface mobility of the Ga atoms with a higher growth temperature and lower TMGa flow, smooth morphologies were achieved on 4H-SiC substrates. Due to the lack of sharp interfaces, the carrier density was lower than expected for this type of structure. Tuning the

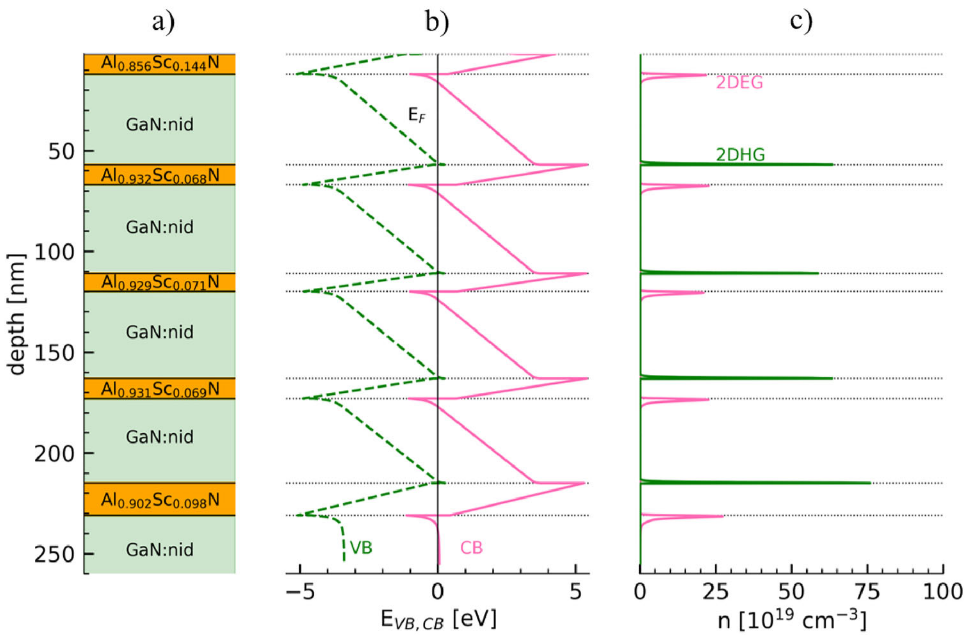

Figure 6. a) Schematic diagram of the five-period AlScN/GaN multichannel heterostructure and the Schrödinger–Poisson 1D simulations of b) the conduction and valence band edges and b) charge carrier distributions of a five-period AlScN/GaN multichannel heterostructure. The thickness and Sc concentrations were taken from the ToF-SIMS results, and the interlayers were neglected.

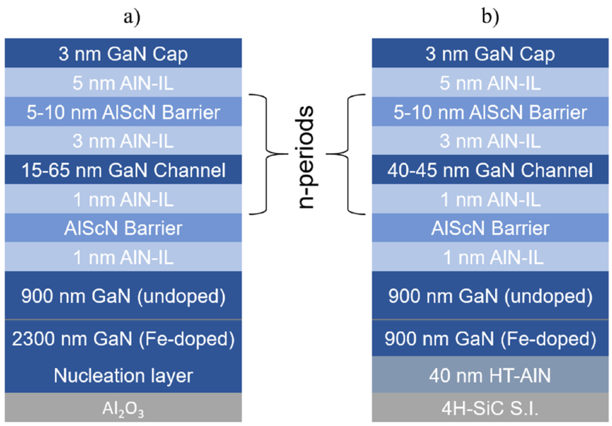

Figure 7. Schematic depiction of an *n*-period (n = 3, 5, 10) AlScN/GaN multichannel heterostructure on a) Al_2O_3 and b) 4H-SiC substrates.

Sc concentration is a challenging task due to the diffusion effect; despite this, a consistent Sc composition was achieved. The ten-period heterostructure cracked as a result of strain, highlighting the sensitivity to deviations from the lattice match concentrations for the growth of this type of structure. The optimum conditions for a five-period heterostructure were found to be a 40 nm thick GaN channel and a ≈10 nm AlScN barrier with a Sc-content of ≈8%. These were deposited on 4H-SiC substrates and exhibited smooth morphologies (surface roughness below 1 nm in a 10×10 μm^2 area) and good structural quality. The five-period multilayer presented a sheet resistance of 129 Ω sq^{-1}, carrier densities of 2.5 × 10^{13} m^{-2}, and mobility of 1911 cm^2 V^{-1} s^{-1}, further cementing the advantages of exploring AlScN-based layers for high-power and high-frequency applications. The presented results reinforce the importance of developing novel HEMTs based on AlScN. As such, selected heterostructures will be processed, and the device performance explored.

5. Experimental Section

AlScN/GaN multichannel heterostructures were grown in a commercial multi-wafer close-coupled showerhead Aixtron MOCVD reactor with a Fraunhofer IAF-patented setup[64] for epitaxial growth with low vapor pressure precursors, previously detailed by Leone et al.[65,66] The heterostructures were grown on 4-inch 0.3 ° off-axis *c*-plane Al_2O_3 substrates or nominally on-axis semi-insulating 4H-SiC substrates. The precursor used for Sc was bis(ethylcyclopentadienyl) (N,N'-bis (dimethylamino) acetamidinato) scandium $(EtCp)_2Sc(bdma)$, supplied by Dockweiler Chemicals GmbH. The sources for Al, Ga, and N were Trimethylaluminum (TMAl), Trimethylgallium (TMGa), and ammonia (NH_3), respectively. Purified hydrogen and nitrogen were employed as carrier gases for the heterostructures, with the latter used for the growth of the GaN channel layers and the final GaN cap.

The starting point of the epilayer stack was the same as that described in previous works.[67–69] For epilayers on 4H-SiC substrates, the growth process started with an AlN nucleation layer, while for Al_2O_3 a low-temperature GaN was initially grown. The GaN buffer structure was a Fe-doped GaN layer to compensate background donor concentrations and a non-intentionally doped GaN layer, which prevented Fe-diffusion into the barrier and acted as the channel[52]. **Figure 7** illustrates the structure of the grown samples for Al_2O_3 and 4H-SiC SI substrates.

Growing GaN layers on top of AlScN was a non-trivial task, as the MOCVD growth conditions required by the two materials differed significantly, and GaN tended to grow three-dimensionally onto AlScN. Recently, Streicher et al.[51] successfully demonstrated the growth of GaN layers on top of AlScN barrier layers. 2D GaN could be grown on AlScN considering the following: 1) introduction of an AlN interlayer (IL) between GaN and AlScN to get better interface abruptness; 2) use of nitrogen as the carrier gas to avoid etching of the surface during the GaN layer growth; 3) increased growth temperature for the GaN layer to enhance the surface mobility of the Ga atoms; and 4) tuning of supersaturation of the gas phase chemistry to attain a low growth rate. By achieving smooth surfaces, it became possible to explore the growth of multiple stacked layers.

The low supersaturation, high temperature, low pressure, and high V/III approach was used to grow the GaN channels. Due to the high growth temperature of the GaN channels, an inert gas as N_2, was needed as the carrier gas to avoid etching. Considering this and anticipating etching effects, N_2 was then used as the carrier gas for the AlScN barriers, except for the first AlScN barrier grown with H_2 as the carrier gas. The AlScN barrier was grown under our typical conditions described previously in other papers,[67,68] with a growth temperature of 1100 °C. A GaN cap layer was grown on top of all heterostructures to prevent surface oxidation.

An AlN IL was added between the AlScN layers, the GaN channels, and the GaN cap, as it helps achieve a better 2DEG confinement, besides making the interfaces more abrupt between the layers. The target thickness of these interlayers was 1–2 nm; however, due to the strong atom diffusion between the layers, an absolute value cannot be stated. This diffusion effect was previously discussed,[19] and led to a barrier with a graded composition of AlGaScN, hence increased alloy scattering can be expected. This effect was reduced by spatially separating the 2DEG from the barrier with the AlN ILs. Likewise, the potential barrier was raised by the high bandgap of AlN, and the n_s was further enhanced by the increased polarization discontinuities.[19,60] Note that, as these ILs were still very thin (< 5 nm) and due to interdiffusion, their composition was not binary, and it was not possible to resolve their actual thickness with SIMS measurements, which is why the value is not shown in Figure 7.

The surface morphology and root mean square roughness (RMS) of the samples were examined by atomic force microscopy (AFM) in tapping mode. The chemical composition of the layers was studied by depth profiling with time-of-flight secondary ion mass spectrometry (ToF-SIMS) using an M6 Plus instrument (IONTOF GmbH, Germany). The ToF-SIMS instrument operated in dual-beam mode, employing a 1 keV Cs^+ sputter beam along with a 30 keV $Bi_1{}^+$ primary beam for crater analysis, both incident at an angle of 45°. The Sc concentration was determined with the help of magnetron-sputtered AlScN reference samples, previously calibrated through time-of-flight energy elastic recoil detection analysis (ToF-ERDA).[70] The thickness of the layers was determined by measuring the crater depth with an integrated scanning probe microscope (SPM). High-resolution X-ray diffractometry (HRXRD) Θ/2Θ-scans of the 0002, 0004, and 0006 reflection ranges combined with X-ray reflectometry (XRR) and HRXRD reciprocal space mappings (RSM) of the 11$\bar{2}$4-reflection ranges were used to assess the crystalline quality, the super lattice period, and the strain (RSM) of the heterostructures. These measurements were carried out with a Rigaku SmartLab multipurpose diffractometer system.

A cross-section specimen of the multilayer GaN-channel/AlScN-barrier/AlN-IL structure on Al_2O_3 was prepared using a novel "flying cube"-strategy capable of preparing high-quality cross-section samples from non- or poorly conductive layers within a short time and with fewer milling artifacts using the focused-ion-beam (FIB) technique.[53] After electron beam-induced (ebid) Pt-deposition for better TEM contrast at the sample surface, a thin Si-Cube was placed on top for high-quality lamella preparation. The lift-out and thinning procedures were performed on a ThermoFisher Helios G4 Plasma FIB CXe system. Scanning transmission electron microscopy (STEM) investigation was conducted on a probe C_s aberration-corrected (CEOS, ASCOR) microscope (JEOL, NEOARM) operated at 200 kV. Imaging of the multilayer structure and atomic structure across individual interfaces was performed using the high-angle annular dark-field (HAADF)-STEM and annular bright-field (ABF) detectors. The effect of sample drift and scan distortions was reduced by serial image acquisition (≈5–8 images, 1024×1024 px, 4 μs dwell time) and non-rigid image alignment using the SmartAlign (HREM Research, Inc.) plug-in for Digital Micrograph (Gatan, Inc.).[71] Additionally, a Fourier filter was applied to remove higher frequency noise (HREM-Filters Pro/Lite v.4.2.1, HREM Research, Inc.). The strain distribution across the multiple-channel heterostructure was evaluated using the geometric phase analysis (GPA) algorithm on multi-frame data sets (≈30 images, 2048×2048 px, 1.5 µs dwell time).[54] The chemical distribution across individual layers was mapped by energy-dispersive X-ray spectroscopy (EDS), collecting the signal with a dual silicon drift detector system (JEOL, active area 100 mm^2 per detector).

All heterostructures were electrically characterized at room temperature (RT) using eddy-current sheet resistance measurements and contactless Hall measurements with a Semilab contactless mobility mapper. For this effect, 17 measurement points evenly distributed throughout the wafer were used to determine the average values from the transport properties: sheet resistance (R_{sh}), carrier density (n_s), and mobility (µ).

The 1D Schrödinger–Poisson equation solver nextnano^{++} was used to simulate the conduction and valence band edges, and to calculate the theoretical charge carrier distributions of electrons and holes of the heterostructures.[72] The information on the chemical composition needed for these simulations was obtained from the ToF-SIMS measurements. A Schottky barrier height of $\phi_B = 1.4$ eV was chosen as the boundary condition for the simulation, a value that was determined for MBE-grown AlGaN/GaN.[73] It was also widely accepted to approximate the Schottky barrier height to one-third of the bandgap of the topmost material.[74] For a GaN-capped sample, this would be around 1.13 eV. According to simulations, the Schottky barrier height affected only the topmost 2DEG, and did not impact the underlying ones. The structure was undoped, metal-polar, and the temperature of the simulation was set to 300 K.

Supporting Information

Supporting Information is available from the Wiley Online Library or from the author.

Acknowledgements

The Fraunhofer authors acknowledge Dockweiler Chemicals GmbH for supplying the Sc precursor used for this study. The authors thank Hanspeter Menner, Christian Manz, and Stefan Müller for their support with sample preparation and characterization.

Open access funding enabled and organized by Projekt DEAL.

Conflict of Interest

The authors declare no conflict of interest.

Data Availability Statement

The data that support the findings of this study are available from the corresponding author upon reasonable request.

Keywords

III-N heterostructures, AlScN, epitaxy, GaN, HEMT, MOCVD, multichannel

Received: August 8, 2025
Revised: September 19, 2025
Published online:

[1] R. Quay, D. Schwantuschke, E. Ture, F. van Raay, C. Friesicke, S. Krause, S. Müller, S. Breuer, B. Godejohann, P. Brückner, *Phys. Status Solidi A* **2018**, *215*, 1700655.
[2] X. Ding, Y. Zhou, J. Cheng, *CES Trans. Electr. Mach. Systems* **2019**, *3*, 54.
[3] M. Meneghini, C. De Santi, I. Abid, M. Buffolo, M. Cioni, R. A. Khadar, L. Nela, N. Zagni, A. Chini, F. Medjdoub, G. Meneghesso, G. Verzellesi, E. Zanoni, E. Matioli, *J. Appl. Phys.* **2021**, *130*, 18.
[4] S. Heikman, S. Keller, D. S. Green, S. P. DenBaars, U. K. Mishra, *J. Appl. Phys.* **2003**, *94*, 5321.
[5] J. Ma, C. Erine, P. Xiang, K. Cheng, E. Matioli, *Appl. Phys. Lett.* **2018**, *113*, 24.
[6] C. Erine, J. Ma, G. Santoruvo, E. Matioli, *IEEE Electron Device Lett.* **2020**, *41*, 321.
[7] M. Xiao, Y. Ma, K. Cheng, K. Liu, A. Xie, E. Beam, Y. Cao, Y. Zhang, *IEEE Electron Device Lett.* **2020**, *41*, 1177.
[8] M. Xiao, Y. Ma, K. Liu, K. Cheng, Y. Zhang, *IEEE Electron Device Lett.* **2021**, *42*, 808.
[9] Y. Cao, K. Wang, G. Li, T. Kosel, H. Xing, D. Jena, *J. Cryst. Growth* **2011**, *323*, 529.
[10] H. Li, Y. Wang, Q. Xie, H. Xie, H. T. Tan, P. Dalapati, S. Liu, K. Ranjan, S. Foo, S. Arulkumaran, C. Lip Gan, G. Ing Ng, *Appl. Phys. Express* **2025**, *18*, 016502.
[11] D. Crippa, G. L. Valente, A. Ruggiero, L. Neri, R. Reitano, L. Calcagno, G. Foti, M. Mauceri, S. Leone, G. Pistone, et al., in *Mater. Sci. Forum*, vol. *483*, Trans Tech Publ, **2005**, pp. 67–72.
[12] F. La Via, G. Galvagno, F. Roccaforte, F. Giannazzo, S. Di Franco, A. Ruggiero, R. Reitano, L. Calcagno, G. Foti, M. Mauceri, S. Leone, G. Pistone, F. Portuese, G. Abbondanza, G. Abbagnale, A. Veneroni, F. Omarini, L. Zamolo, M. Masi, G. L. Valente, D. Crippa, *Microelectron. Eng.* **2006**, *83*, 48.
[13] H. Pedersen, S. Leone, O. Kordina, A. Henry, S.-i. Nishizawa, Y. Koshka, E. Janzén, *Chem. Rev.* **2012**, *112*, 2434.
[14] A. Henry, S. Leone, F. C. Beyer, H. Pedersen, O. Kordina, S. Andersson, E. Janzén, *Phys. B* **2012**, *407*, 1467.
[15] P. Sohi, J. Carlin, M. Rossell, R. Erni, N. Grandjean, E. Matioli, *Semicond. Sci. Technol.* **2021**, *36*, 055020.
[16] A. Li, C. Wang, S. Xu, X. Zheng, Y. He, X. Ma, X. Lu, J. Zhang, K. Liu, Y. Zhao, Y. Hao, *Appl. Phys. Lett.* **2021**, *119*, 12.
[17] J.-F. Carlin, M. Ilegems, *Appl. Phys. Lett.* **2003**, *83*, 668.
[18] R. Butté, J. Carlin, E. Feltin, M. Gonschorek, S. Nicolay, G. Christmann, D. Simeonov, A. Castiglia, J. Dorsaz, H. Buehlmann, S. Christopoulos, G. B. H. von Högersthal, A. J. D. Grundy, M. Mosca, C. Pinquier, M. A. Py, F. Demangeot, J. Frandon, P. G. Lagoudakis, J. J. Baumberg, N. Grandjean, *J. Phys. D: Appl. Phys.* **2007**, *40*, 6328.
[19] I. Streicher, S. Leone, C. Manz, L. Kirste, M. Prescher, P. Waltereit, M. Mikulla, R. Quay, O. Ambacher, *Cryst. Growth Des.* **2023**, *23*, 782.
[20] S. Fichtner, N. Wolff, F. Lofink, L. Kienle, B. Wagner, *J. Appl. Phys.* **2019**, *125*, 11.
[21] J. Wang, M. Park, S. Mertin, T. Pensala, F. Ayazi, A. Ansari, *J. Microelectromech. Syst.* **2020**, *29*, 741.
[22] N. Wolff, G. Schönweger, M. R. Islam, Z. Ding, C. Kübel, S. Fichtner, L. Kienle, *Adv. Sci.*, e03827.
[23] J. X. Zheng, M. M. A. Fiagbenu, G. Esteves, P. Musavigharavi, A. Gunda, D. Jariwala, E. A. Stach, R. H. Olsson, *Appl. Phys. Lett.* **2023**, *122*, 22.
[24] G. Giribaldi, L. Colombo, M. Rinaldi, *IEEE Trans. Ultrason. Ferroelectr. Freq. Control* **2023**, *70*, 1201.
[25] A. Dadgar, F. Hörich, R. Borgmann, J. Bläsing, G. Schmidt, P. Veit, J. Christen, A. Strittmatter, *Phys. Status Solidi A* **2023**, *220*, 2200609.
[26] K. Pingen, A. M. Hinz, P. Sandström, N. Wolff, L. Kienle, L. Scipioni, J. Greer, E. von Hauff, L. Hultman, J. Birch, C.-L. Hsiao, *Vacuum* **2024**, *220*, 112852.
[27] J. Casamento, C. S. Chang, Y.-T. Shao, J. Wright, D. A. Muller, H. G. Xing, D. Jena, *Appl. Phys. Lett.* **2020**, *117*, 11.
[28] J. Casamento, H. G. Xing, D. Jena, *Phys. Status Solidi (b)* **2020**, *257*, 1900612.

[29] J. Casamento, H. Lee, T. Maeda, V. Gund, K. Nomoto, L. van Deurzen, W. Turner, P. Fay, S. Mu, C. G. Van de Walle, A. Lal, H. (Grace) Xing, D. Jena, *Appl. Phys. Lett.* **2022**, *120*, 15.
[30] P. Wang, D. A. Laleyan, A. Pandey, Y. Sun, Z. Mi, *Appl. Phys. Lett.* **2020**, *116*, 15.
[31] P. Wang, D. Wang, N. M. Vu, T. Chiang, J. T. Heron, Z. Mi, *Appl. Phys. Lett.* **2021**, *118*, 22.
[32] P. Wang, D. Wang, S. Mondal, Z. Mi, *Appl. Phys. Lett.* **2022**, *121*, 2.
[33] V. Gund, B. Davaji, H. Lee, J. Casamento, H. G. Xing, D. Jena, A. Lal, in *2021 21st Int. Conf. on Solid-State Sensors, Actuators and Microsystems (Transducers)*, IEEE, Piscataway, NJ **2021**, pp. 1064–1067.
[34] D. Wang, P. Wang, S. Mondal, S. Mohanty, T. Ma, E. Ahmadi, Z. Mi, *Adv. Electron. Mater.* **2022**, *8*, 2200005.
[35] J. Casamento, K. Nomoto, T. Nguyen, H. Lee, C. Savant, L. Li, A. Hickman, T. Maeda, J. Encomendero, V. Gund, A. Lal, J. C. M. Hwang, H. G. Xing, D. Jena, in *2022 Int. Electron Devices Meeting (IEDM)*, IEEE, Piscataway, NJ **2022**, pp. 11–1.
[36] M. Park, Z. Hao, R. Dargis, A. Clark, A. Ansari, *J. Microelectromech. Syst.* **2020**, *29*, 490.
[37] V. Gund, K. Nomoto, H. G. Xing, D. Jena, A. Lal, in *2022 IEEE Int. Symp. on Applications of Ferroelectrics (ISAF)*, IEEE, Piscataway, NJ **2022**, pp. 1–4.
[38] M. T. Hardy, B. P. Downey, N. Nepal, D. F. Storm, D. S. Katzer, D. J. Meyer, *ECS Trans.* **2017**, *80*, 161.
[39] M. T. Hardy, B. P. Downey, N. Nepal, D. F. Storm, D. S. Katzer, D. J. Meyer, *Appl. Phys. Lett.* **2017**, *110*, 16.
[40] M. B. Tahhan, J. A. Logan, M. T. Hardy, M. G. Ancona, B. Schultz, B. Appleton, T. Kazior, D. J. Meyer, E. M. Chumbes, *IEEE Trans. Electron Devices* **2022**, *69*, 962.
[41] K. Nomoto, J. Casamento, T.-S. Nguyen, L. Li, H. Lee, C. Savant, A. L. Hickman, T. Maeda, J. Encomendero, V. Gund, T. Vasen, S. Afroz, D. Hannan, J. C. M. Hwang, D. Jena, H. G. Xing, *Appl. Phys. Express* **2025**, *18*, 016506.
[42] B. Dzuba, T. Nguyen, A. Sen, R. E. Diaz, M. Dubey, M. Bachhav, J. P. Wharry, M. J. Manfra, O. Malis, *J. Appl. Phys.* **2022**, *132*, 17.
[43] L. Van Deurzen, T.-S. Nguyen, J. Casamento, H. Xing, D. Jena, *Appl. Phys. Lett.* **2023**, *123*, 24.
[44] T.-S. Nguyen, N. Pieczulewski, C. Savant, J. J. Cooper, J. Casamento, R. S. Goldman, D. A. Muller, H. G. Xing, D. Jena, *APL Mater.* **2024**, *12*, 10.
[45] S. Leone, J. Ligl, C. Manz, L. Kirste, T. Fuchs, H. Menner, M. Prescher, J. Wiegert, A. Žukauskaitė, R. Quay, O. Ambacher, *Phys. Status Solidi RRL* **2020**, *14*, 1900535.
[46] X. Laufenberg, Eynius, Method and apparatus for manufacturing a semiconductor layer and substrate provided therewith.
[47] N. Wolff, G. Schönweger, I. Streicher, M. R. Islam, N. Braun, P. Straňák, L. Kirste, M. Prescher, A. Lotnyk, H. Kohlstedt, S. Leone, L. Kienle, S. Fichtner, *Adv. Phys. Res.* **2024**, *3*, 2300113.
[48] C. Moe, R. Olsson, P. Patel, Z. Tang, M. D'Agati, M. Winters, R. Vetury, J. Shealy, in *2020 IEEE Int. Ultrasonics Symp. (IUS)*, IEEE, Piscataway, NJ **2020**, pp. 1–4.
[49] C. G. Moe, J. Leathersich, D. Carlstrom, F. Bi, D. Kim, J. B. Shealy, *Phys. Status Solidi A* **2023**, *220*, 2200849.
[50] S. Krause, I. Streicher, P. Waltereit, L. Kirste, P. Brückner, S. Leone, *IEEE Electron Device Lett.* **2022**, *44*, 17.
[51] I. Streicher, N. Wolff, T. Duarte, O. Rehm, P. Straňák, L. Kirste, M. Prescher, X. Guo, V. Nicolosi, L. Baumgarten, M. Müller, L. Kienle, S. Leone, *Adv. Phys. Res.* **2025**.
[52] S. Leone, F. Benkhelifa, L. Kirste, C. Manz, S. Mueller, R. Quay, T. Stadelmann, *Phys. Status Solidi (b)* **2018**, *255*, 1700377.
[53] S. Beuer, M. Rommel, in *2024 IEEE Int. Symp. on the Physical and Failure Analysis of Integrated Circuits (IPFA)*, IEEE, Piscataway, NJ **2024**, pp. 01–04.
[54] L. Jones, S. Wenner, M. Nord, P. H. Ninive, O. M. Løvvik, R. Holmestad, P. D. Nellist, *Ultramicroscopy* **2017**, *179*, 57.
[55] L. Calcagno, G. Izzo, G. Litrico, G. Foti, F. La Via, G. Galvagno, M. Mauceri, S. Leone, *J. Appl. Phys.* **2007**, *102*, 4.
[56] S. Leone, H. Pedersen, A. Henry, O. Kordina, E. Janzén, in *Mater. Sci. Forum*, vol. *600*, Trans Tech Publ, **2009**, pp. 107–110.
[57] S. Leone, F. C. Beyer, A. Henry, O. Kordina, E. Janzén, *Phys. Status Solidi RRL* **2010**, *4*, 305.
[58] S. Leone, F. Beyer, H. Pedersen, O. Kordina, A. Henry, E. Janzén, *Mater. Res. Bull.* **2011**, *46*, 1272.
[59] S. Leone, F. Benkhelifa, L. Kirste, C. Manz, R. Quay, O. Ambacher, *J. Appl. Phys.* **2019**, *125*, 23.
[60] I. Streicher, S. Leone, M. Zhang, T. S. Tlemcani, M. Bah, P. Straňák, L. Kirste, M. Prescher, A. Yassine, D. Alquier, O. Ambacher, *Adv. Funct. Mater.* **2024**, 2403027.
[61] A. J. Green, N. Moser, N. C. Miller, K. J. Liddy, M. Lindquist, M. Elliot, J. K. Gillespie, R. C. Fitch, R. Gilbert, D. E. Walker, E. Werner, A. Crespo, E. Beam, A. Xie, C. Lee, Y. Cao, K. D. Chabak, *IEEE Electron Device Lett.* **2020**, *41*, 1181.
[62] T.-S. Nguyen, C. Savant, A. Asteris, H. G. Xing, D. Jena, *Appl. Phys. Lett.* **2025**, *127*, 10.
[63] L. Nela, J. Ma, C. Erine, P. Xiang, T.-H. Shen, V. Tileli, T. Wang, K. Cheng, E. Matioli, *Nat. Electron.* **2021**, *4*, 284.
[64] S. Leone, C. Manz, H. Menner, J. Wiegert, J. Ligl, Method and apparatus for manufacturing a semiconductor layer and substrate provided therewith.
[65] S. Leone, J. Ligl, C. Manz, L. Kirste, T. Fuchs, H. Menner, M. Prescher, J. Wiegert, A. Žukauskaitė, R. Quay, O. Ambacher, *Phys. status solidi (RRL) – Rapid Res. Lett.* **2020**, *14*, 1900535.
[66] S. Leone, I. Streicher, M. Prescher, P. Straňák, L. Kirste, *Phys. Status Solidi RRL* **2023**, *17*, 2300091.
[67] I. Streicher, S. Leone, L. Kirste, C. Manz, P. Straňák, M. Prescher, P. Waltereit, M. Mikulla, R. Quay, O. Ambacher, *PSS RLL* **2022**, *17*.
[68] C. Manz, S. Leone, L. Kirste, J. Ligl, K. Frei, T. Fuchs, M. Prescher, P. Waltereit, M. A. Verheijen, A. Graff, M. Simon-Najasek, F. Altmann, M. Fiederle, O. Ambacher, *Semicond. Sci. Technol.* **2021**, *36*, 034003.
[69] J. Ligl, S. Leone, C. Manz, L. Kirste, P. Doering, T. Fuchs, M. Prescher, O. Ambacher, *J. Appl. Phys.* **2020**, *127*, 19.
[70] A. Zukauskaite, G. Wingqvist, J. Palisaitis, J. Jensen, P. O. Persson, R. Matloub, P. Muralt, Y. Kim, J. Birch, L. Hultman, *J. Appl. Phys.* **2012**, *111*, 9.
[71] L. Jones, H. Yang, T. J. Pennycook, M. S. Marshall, S. Van Aert, N. D. Browning, M. R. Castell, P. D. Nellist, *Adv. Struct. Chem. Imaging* **2015**, *1*, 1.
[72] S. Birner, nextnano - Software for semiconductor nanodevices, https://www.nextnano.de/, February **2025**.
[73] I. Smorchkova, C. Elsass, J. Ibbetson, R. Vetury, B. Heying, P. Fini, E. Haus, S. DenBaars, J. Speck, U. Mishra, *J. Appl. Phys.* **1999**, *86*, 4520.
[74] O. Ambacher, B. Christian, M. Yassine, M. Baeumler, S. Leone, R. Quay, *J. Appl. Phys.* **2021**, *129*, 20.